



Atomic H^{*} mediated fast decontamination of antibiotics by bubble-propelled magnetic iron-manganese oxides core-shell micromotors

Heng Ye^{a,b}, Shengnan Wang^b, Yong Wang^b, Peiting Guo^b, Liying Wang^b, Chengke Zhao^b,
Shuqing Chen^b, Yimai Chen^b, Hongqi Sun^c, Shaobin Wang^{d,*}, Xing Ma^{b,e,**}

^a GEM Co., Ltd., Shenzhen 518101, China

^b Flexible Printed Electronic Technology Center and School of Materials Science and Engineering, Harbin Institute of Technology (Shenzhen), Shenzhen 518055, China

^c School of Science, Edith Cowan University, Joondalup, WA 6027, Australia

^d School of Chemical Engineering and Advanced Materials, The University of Adelaide, SA 5005, Australia

^e Shenzhen Bay Laboratory, No. 9 Duxue Road, Shenzhen 518050, China

ARTICLE INFO

Keywords:

MnO₂ micromotors

Fenton reaction

Catalytic degradation

Adsorptive bubbles separation

Antibiotic removal

ABSTRACT

Wastewater remediation using micro/nanomotors is a hot topic, and MnO₂ based materials have become fascinating alternatives to rare noble metal-based micro/nanomotors. Herein, we demonstrate facile and large-scale synthesis of Fe-MnO₂ core-shell micromotors for antibiotic pollutant removal. Heat-treatment results in a phase transformation of MnO₂ with formation of iron oxides and partially exfoliates the MnO₂ nanoplate shell structure to promote mobility. The iron-manganese oxide micromotors exhibit an efficient removal of tetracycline antibiotics via a combination of catalytic degradation and adsorptive bubble separation. For the first time, atomic H^{*} was found to participate in the micromotor-assisted degradation process, resulting in optimal Fenton reaction in neutral conditions with a good decontamination performance. Owing to the merits of abundance, magnetic recovery, facile fabrication, good motion, and environmental friendliness, as well as decontamination performance in a wide pH range, these core-shell micromotors demonstrate a promising candidate in practical wastewater treatment.

1. Introduction

Micro/nanomotors (MNM)s have received increasing attention in the last two decades because of their small-scale movement and task-performing capability [1–3]. Currently, there are two major applications of MNMs in, e.g., biomedical and environmental fields [4]. Thanks to the enhanced mass transfer and micro-contact of the remediation agents and pollutants by the motion-induced micro-mixing, traditionally diffusion-limited wastewater treatment efficiency can be enhanced by over 12 times with the help of MNMs [5]. Researchers demonstrated various MNMs based environmental remediation strategies for various contaminants, such as oil [6], heavy metals [7], microorganisms [8], and even emerging microplastics [9].

Previously, environmental remediation by catalytic motors mainly relied on the high catalytic activity of platinum (Pt) to trigger small-scale movement [10]. Due to the need for directional motion, most of

these self-propellers have an asymmetrical structure [11]. Thus, special equipment and sophisticated fabrication routes are usually needed to break the resulting particles' symmetry. These fabrication methods include porous template-assisted growth [12], physical vapor deposition [13], and microfluidic fabrication [14]. Although good remediation performance and enhanced autonomous movement were achieved, the high cost of synthetic materials, sophisticated construction routes, low production yield, and deactivation impeded further applications of Pt-based MNMs [15].

In recent years, manganese oxide-based MNMs have shown excellent potential to replace Pt-based catalytic motors for environmental cleaning [16]. These manganese oxide-based motors have the advantages of robust motion, low-cost, facile and scalable fabrication, and multiple environmental functionalities [9]. These merits are especially favorable for practical environmental cleaning scenarios. Fenton reaction-based oxidative removals of organic pollutants are widely studied to

* Corresponding author.

** Corresponding author at: Flexible Printed Electronic Technology Center and School of Materials Science and Engineering, Harbin Institute of Technology (Shenzhen), Shenzhen 518055, China.

E-mail addresses: shaobin.wang@adelaide.edu.au (S. Wang), maxing@hit.edu.cn (X. Ma).

<https://doi.org/10.1016/j.apcatb.2022.121484>

Received 22 February 2022; Received in revised form 26 April 2022; Accepted 5 May 2022

Available online 7 May 2022

0926-3373/© 2022 Elsevier B.V. All rights reserved.

decontaminate various organic pollutants [17]. Combining MnO_2 based catalytic MNMs with the Fenton reaction may lead to highly efficient environmental remediation.

Liu et al. fabricated iron-containing tubular micromotors for catalytic degradation of organics [18]. They also demonstrated the environmental decontamination applications of these tubular micromotors with a MnO_2 based catalyst [19]. Villa et al. established template-fabricated tubular motors with MnO_2 as the catalyst for organics and heavy metal removals [16]. Pt-free metal oxides-based MNMs have great potential to solve practical problems; especially the micromotors avoid using the porous template-assisted fabrication and physical vapor depositions [20]. These two approaches usually have a prohibitive fabrication cost and production yield for practical wastewater treatment applications. Hence, metal oxide-based low-cost MNMs are on the rise, especially manganese oxide-based micromotors. Liu et al. designed the cotton fiber templated tubular motors with MnO_2 as the catalyst for propulsion and adsorptive removal of organic pollutants [21]. He et al. designed carbon/ MnO_2 for adsorption removal of silver ions and methylene blue [22]. Escarpa and coworkers designed the tubular MnO_2 based micromotors for dyes and chlorophenols degradation [23]. Hence, future development of MNMs in environmental cleaning should focus on MnO_2 based MNMs with facile and large-scale production. Previously, we designed iron oxides- MnO_2 core-shell motors for organics and microplastics removal [9]. The low generation of reactive catalytic radicals by iron oxides takes too long for these motors to degrade organic dyes.

Antibiotics have been widely applied to treat infectious diseases caused by microbes. Antibiotics-induced water pollution has obtained a significant concern from the scientific community and the public [24–26]. Extensive uses of antibiotics in disease treatment and prevention for humans and livestock farming inevitably result in their release into the ecosystem, leading to the generation of antibiotic-resistant bacteria and antibiotic-resistant genes, which have caused a significant threat to the ecological system and human health [27]. It is imperative to design appropriate elimination protocols to remove the antibiotics from polluted water [28–30].

Although electron paramagnetic resonance (EPR) based methods for radicals testing have been widely studied in environmental investigations to elucidate the contaminant degradation mechanisms [31], they have been rarely connected with the synthetic MNMs based catalytic degradations [32]. The Fenton reaction for reactive oxygen species (ROS) utilization is a widely studied environmental decontamination strategy [32]. Fenton reaction-based advanced oxidation processes (AOPs) are highly efficient in generating hydroxyl radicals ($\cdot\text{OH}$) in the optimal acidic condition with a pH value of around 3 [33]. However, a narrow optimal pH range of the traditional Fenton processes and a large quantity of iron-containing sludge limit the large-scale applications [34]. Hence, it is desirable to simplify the utilization procedures and overcome the secondary pollution from iron-containing sludges. Qu and coworkers developed an electrocatalytic H_2O_2 activation method to generate $\cdot\text{OH}$ by an electrochemical cell with a Pd/graphite cathode to generate atomic H^* in a wide pH range [35]. The lone electron in atomic H^* cleaves the peroxide bridge to generate hydroxyl radicals and water, thus extending the optimal pH range to neutral conditions. Li et al. designed a Cu-based metallic glass catalyst for decontamination of organic dyes [36]. The H^+ would gain electrons in an acidic environment to produce atomic H^* due to the infinite microscopic galvanic cells on the metallic glass surface. The atomic H^* effectively promotes the Fenton reaction by extending the optimal pH range of acidic conditions to higher pH values. As far as we know, no one has ever reported the atomic H^* generation by a micromotor-based catalyst.

Herein, we report the fabrication of a series of magnetic and core-shell iron-containing manganese oxides propelled micromotors using a hydrothermal process followed by calcination. Contrary to previous sophisticated fabrication procedures with an extremely low production yield [16,37], we developed a facile and large-scale production of

bubble propelled catalytic motors. We investigated the heat-treatment process on the motors' morphology and mobility. These Fe- MnO_2 motors also showed fast movement in H_2O_2 fuel with magnetic steering. We evaluated the motors' decontamination for tetracycline antibiotic removal, which revealed that catalytic degradation plays a leading role in the remediation process and that adsorptive bubble separation (ABS) also contributes to pollutant removal. At a higher catalytic MNMs dosage, ABS improves the overall removal efficiency. Under various experimental settings, good catalytic degradation performances were achieved with the hydrothermally synthesized and calcined iron-manganese oxides (FMO) micromotors. In neutral or acid environmental conditions, all these MNMs demonstrate a good decontamination performance. The FMO micromotors show even higher decontaminations in neutral conditions than in acidic conditions due to the generated atomic H^* . This work clarified the involvement of atomic H^* radicals with other radicals for organic degradation. The underlying mechanism explained that the degradation performance improved with a wider pH range. The micromotors-based Fenton reaction shows excellent potential to replace the traditional Fenton reaction with advantages of a lower dosage, higher performance, and wider pH range. The Fe- MnO_2 micromotors-assisted protocols for pollutant remediation show great potential for practical wastewater treatment.

2. Materials and methods

2.1. Materials and chemicals

Spherical iron particles (1 μm in mean diameter) were purchased from Haoxinnano (Shanghai, China). Peroxide solution (H_2O_2 , 30%), hydrochloric acid (37%), potassium permanganate (KMnO_4), sodium hydroxide, Triton-X-100, sodium dodecyl sulfate (SDS), methylene blue (MB), terephthalic acid, and tetracycline (TC) antibiotics were ordered from Aladdin. In addition, 5,5-dimethyl-1-pyrroline N-oxide (DMPO) and 2,2,6,6-tetramethyl-4-piperidinol (TEMP) were purchased from Macklin. All the chemicals were used as received. Deionized water (DI water, $\geq 18.2 \text{ M}\Omega \text{ cm}$) was obtained from a Milli-Q purification system and used in all aqueous solution preparation.

2.2. Experimental procedures

Firstly, we used a simple hydrothermal reaction to prepare the magnetic Fe- MnO_2 catalytic motors [9]. The Fe- MnO_2 core-shell particles were obtained and denoted as the FMO micromotors. Then, we used a furnace to calcine the FMO at different temperature from 300 to 500 $^\circ\text{C}$. The resulting powders were denoted as FMO300, FMO350, FMO380, FMO400, FMO450, and FMO500 micromotors.

X-ray diffraction (XRD) patterns were collected on a SmartLab X-ray diffractometer (Rigaku, Japan). Scanning electron microscopy (SEM) images and energy-dispersive X-ray spectroscopy (EDX) analysis were performed on the field emission SEM (Hitachi S-4700, Japan and Zeiss SUPRA 55, Germany). Magnetization behavior was investigated by a Model PPMS-9 (Quantum Design, USA). A plastic transparent glass-bottomed microwell dish from Cellvis (Mountain View, CA) was used for motion behavior observation [38]. Optical images and videos were taken by a Leica DMI8 microscope. N_2 adsorption-desorption isotherms were conducted on a Quantachrome Autosorb-IQ-MP analyzer (USA). A UV-2600 spectrometer (Shimadzu) was employed to determine TC content. We used a Bruker EPR-E500 (Germany) instrument to perform the EPR tests [39,40]. We also used the terephthalic acid method to examine $\cdot\text{OH}$ generation by FMO micromotors. Detailed experimental procedures are presented in the [supplementary data](#).

3. Results and discussion

3.1. Fabrication and characterizations of iron-manganese oxides micromotors

As presented in Fig. 1a, FMO microparticles were firstly constructed using spherical magnetic iron particles as the core (Fig. S1-S2, supplementary data) for the flower-like MnO_2 nanoplates shell to grow. SEM images in Fig. S1 show that most of the as-received iron micro balls have a spherical shape with smooth surfaces. The XRD pattern in Fig. S2 verifies that the synthetic material is the unoxidized pure α -Fe phase. Then we calcined the FMO motors to tune the surface morphology and crystallinity further. In environmental cleaning processes, catalytic FMO motors generate micro-bubbles and reactive oxygen species (ROS) in large quantities owing to the fast bubbling process and good motion behaviors by the particles' MnO_2 outer layer and the Fenton reaction by the iron-containing catalyst with peroxide. Therefore, the dissolved antibiotic pollutants were separated by the microbubbles and oxidized by the ROS. Fig. 1b shows the remediation mechanism by the bubble propelling FMO core-shell MNMs. The adsorptive bubble separation (ABS) and catalytic degradation mechanism contribute to the overall antibiotic decontamination process.

Fig. 2 shows the typical SEM images and EDS characterization of the FMO micromotors. Fig. 2a shows the smooth surface of the pure iron particle as the synthetic material was covered by the microstructured flower-like nanoplates, resulting in the formation of the core-shell hybrids. A high-resolution image of the nanoplate structure in Fig. 2b shows that these nanoplates are interlinked and perpendicular to the globe center. The MnO_2 nanoplates are wrapped into the well-like hollow structure on the core-shell particle surface, thus facilitating the formation of O_2 bubbles when reacting with peroxide. These concave surface cavities serve as the ideal bubble generation sites, as the concave surface facilitates the generated O_2 molecules to form microbubbles. The

structure of flower-like nanoplates originated from the hydrothermal reaction and greatly enhanced the peroxide decomposition and bubble formation process. Fig. 2g shows the homogeneous distribution of Mn, O, and Fe elements. As presented in Fig. S3, the FMO micromotors lack asymmetry in geometrical shapes. The MnO_2 nanoplates uniformly covered all the surfaces of the iron particles. The round shape and uniform distribution of the MnO_2 nanoplates mean their mobility can be enhanced by partial exfoliation of the MnO_2 nanoplate structure. Fig. 2c-d shows the FMO300 micromotors after the heat-treatment at 300°C for 10 min. We observed that the flower-like MnO_2 nanoplates show a decreasing tendency with the increasing heating temperature. A large quantity of MnO_2 nanoplates were exfoliated from the particle surface, resulting in barer and rounder core-shell motors. High-resolution images in Fig. 2d show that the upper part surface has the MnO_2 nanoplates, while the lower part nanoplates were exfoliated. Fig. S4 presents the SEM images of FMO300 micromotors in large quantities. Fig. S5–9 shows the SEM images of other heat-treated FMO micromotors.

Fig. 2e and S7 show the surface morphology of FMO400 micromotors. We also observed the partial exfoliation of the surface MnO_2 nanoplates. Although the MnO_2 nanoplates were exfoliated greatly, their surface is still quite rough with small convex nanoplates. Fig. 2f and S8 present the SEM image of FMO450 micromotors. Even though we thermally treated these MNMs at 450°C , most MnO_2 nanoplates still exist on the surface. Fig. S8–9 shows that, even at higher temperature calcination, the flower-like nanoplates remained. It seems that the calcination-induced partial exfoliation of the nanoplates would generate a certain degree of structural asymmetry.

The diffraction peaks in Fig. 3a-b demonstrate the influence of heat-treatment processes on the resulting phase composition of micromotors. The original FMO micromotors consist of an iron core and birnessite type δ - MnO_2 shell. The potassium birnessite phase MnO_2 also exists in the hydrothermally synthesized MnO_2 shell, showing the influence of the synthetic material by potassium permanganate. Usually, an

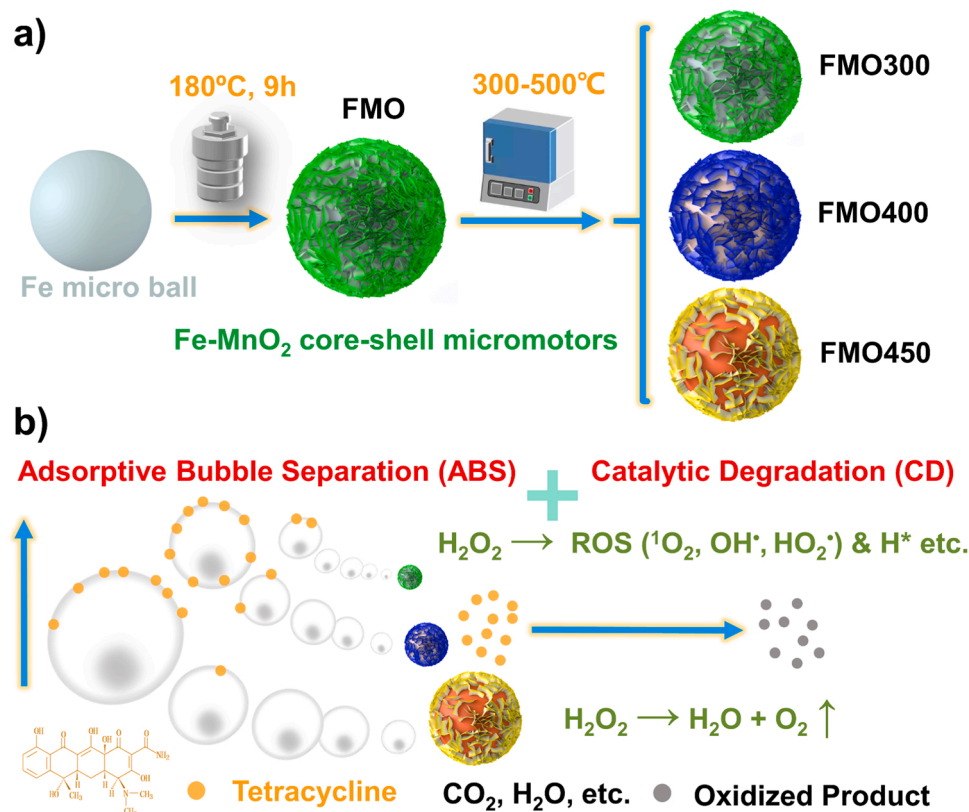


Fig. 1. Schematic illustration of the synthesis and application of the FMO micromotors. (a) fabrication process. (b) Tetracycline antibiotic decontamination mechanism by the FMO micromotors.

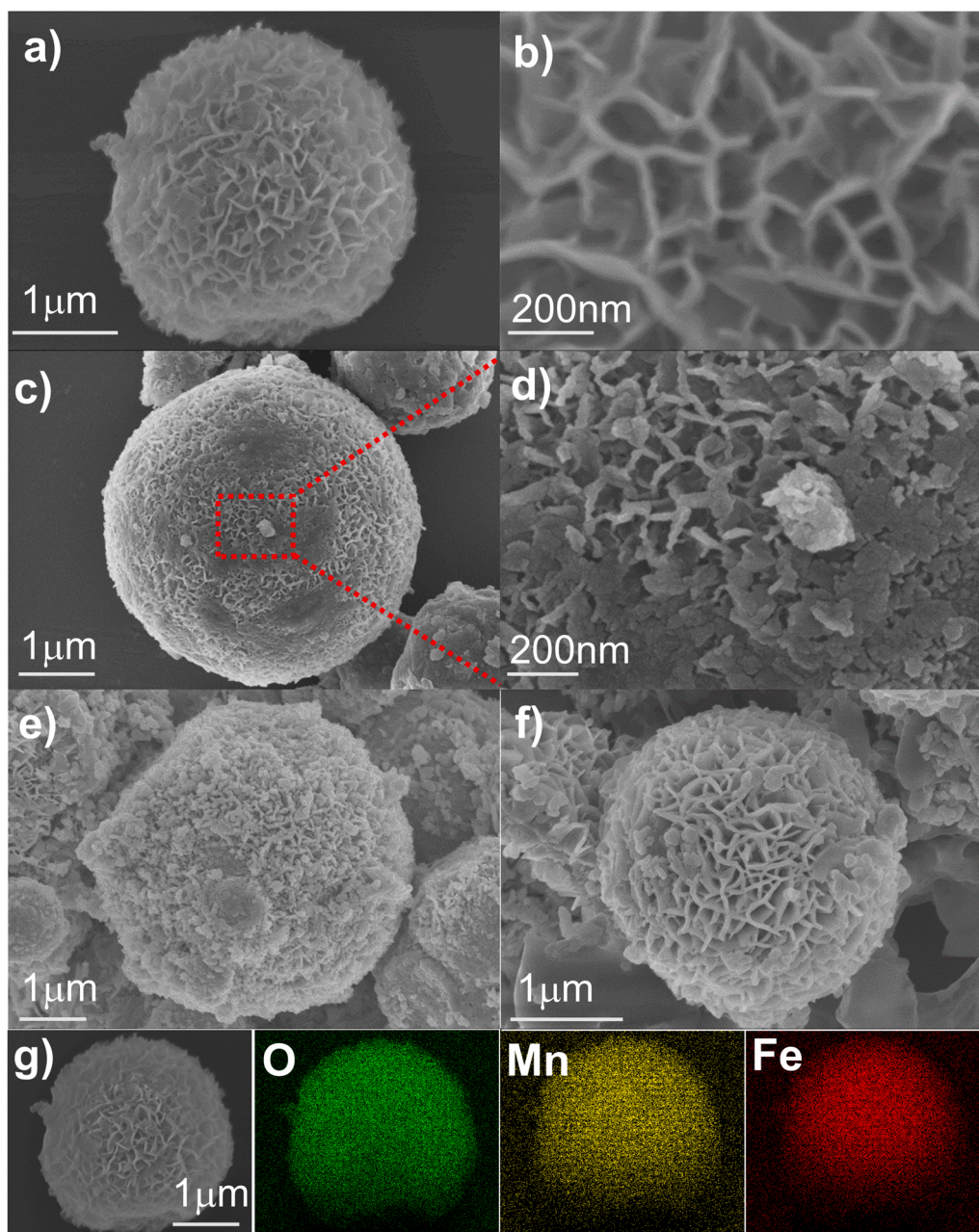


Fig. 2. SEM images: (a), (b) FMO; (c), (d) FMO300; (e) FMO400; (f) FMO450. (g) EDX mapping analysis of an FMO micromotor.

amorphous MnO_2 phase exists in the hydrothermally synthesized sample due to the lack of heat treatment [9]. Besides the amorphous MnO_2 lattices, mainly six types of crystalline MnO_2 phases exist, namely α - MnO_2 , β - MnO_2 , γ - MnO_2 , δ - MnO_2 , ϵ - MnO_2 , and λ - MnO_2 . The birnessite belongs to a δ - MnO_2 phase, whose octahedron $[\text{MnO}_6]$ units form a 2D layered structure, and a 0.7 nm interlayer distance can accommodate small water molecules and metal cations [41]. The K-birnessite MnO_2 is the birnessite MnO_2 by incorporating the potassium cation interlayers. There are many MnO_2 based MNMs developed by now, while no systematic investigation was reported on the effects of different phases on the mobility behavior and decontamination performance [19,22,42,43]. Besides, the geometry shapes of MnO_2 based MNMs vary greatly, adding to the difficulties of systematically evaluating the performance of different types of manganese oxide motors in mobility and decontamination. As shown in Figs. 2 and 3a, the heat-treatment process at 300 °C only results in the exfoliation of surface MnO_2 nanoplates, while no phase structure change occurred.

Fig. 3c shows N_2 sorption tests of FMO and FMO300 micromotors. Based on the IUPAC classification, the motor catalysts demonstrate a type IV isotherm with a type H3 hysteresis loop, indicating the typical mesoporous structure of FMO micromotors [44]. Fig. 3c shows a broad hysteresis loop at a relative pressure range (P/P_0) from 0.4 to 0.95. The hysteresis loop of FMO was much broader than FMO300, which means that the FMO motors have a more porous structure with a larger surface area and pore volume. The specific surface areas (SSAs) of FMO and FMO300 micromotors are 12.5 and 7.2 m^2/g , respectively, and their total pore volumes are 0.045 and 0.031 cm^3/g , respectively. Elevating the temperature to 350 °C, a small portion of a magnetite phase formed. As shown in Fig. 3b, the birnessite MnO_2 transformed to α - MnO_2 at a heating temperature of 450 °C for 10 min. From 350 °C above, a significant amount of Fe_3O_4 phase formed due to the oxidation of iron by atmosphere O_2 . Higher temperature calcination results in more Fe_3O_4 phase formed, as evidenced by the higher diffraction peaks of the magnetite phase. Amorphous MnO_2 transferred to α - MnO_2 at above

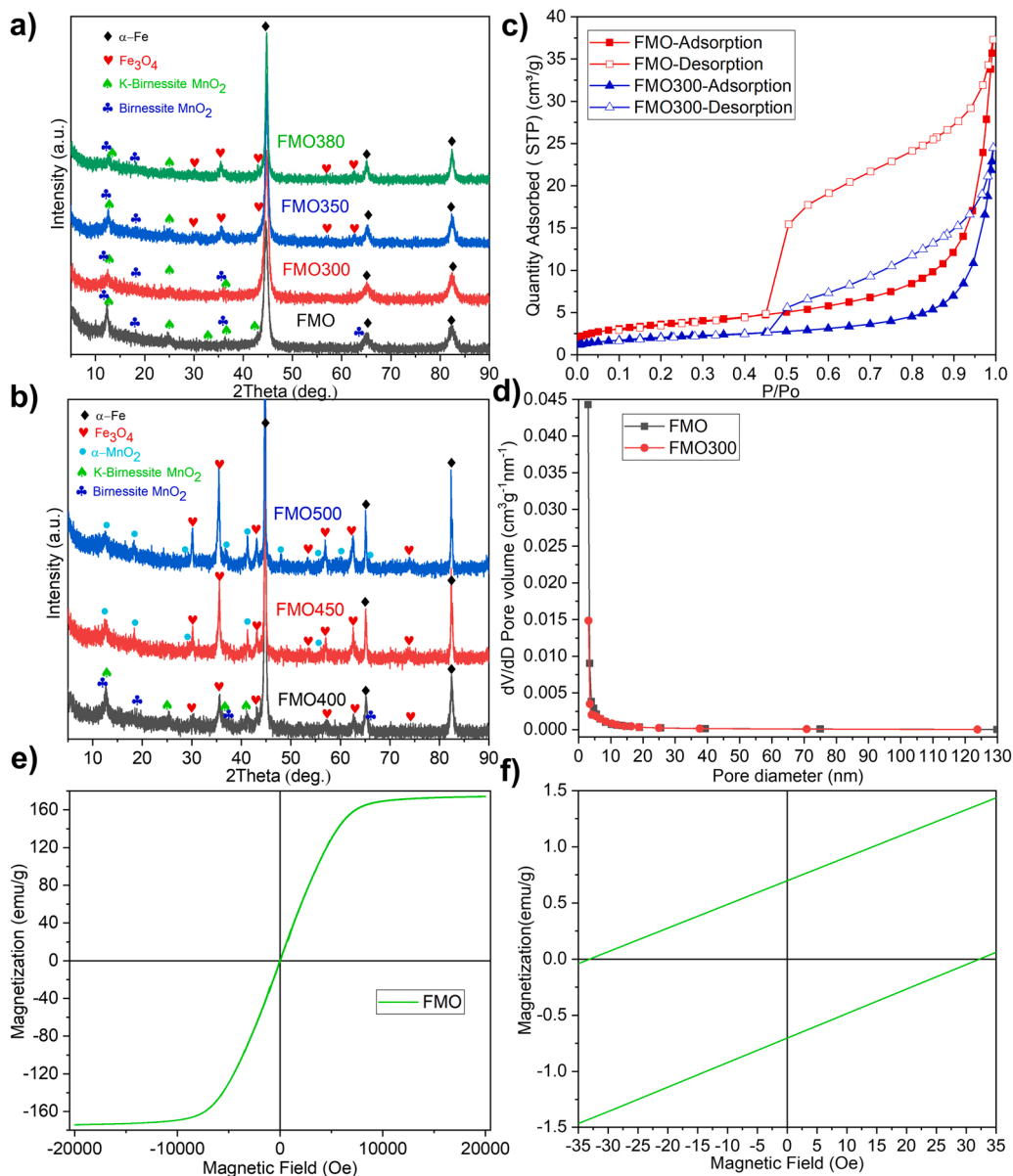


Fig. 3. FMO micromotor characterization: XRD patterns of the iron-manganese oxides micromotors: (a) FMO, FMO300, FMO350, and FMO380; (b) FMO400, FMO450, and FMO500; FMO and FMO300 micromotors' N_2 adsorption (solid symbols)/desorption (open symbols) isotherms (c) and pore size distribution (d); Magnetization behavior of the FMO micromotors (e) and the enlargement of hysteresis loop at low magnetic fields (f).

450 °C. As shown by Fig. 3e, the FMO micromotors present saturation magnetization of 174.02 emu/g, significantly larger than our previously developed micromotors with values of 45.75 and 20.89 emu/g [9], demonstrating the excellent magnetic steering ability. Fig. 3f shows that the coercivity is 33 Oe and the remanent magnetization is 0.7 emu/g, indicating a typical soft ferromagnetic characteristic. We believe that the FMO micromotors swarm can be activated by an external rotating magnetic field. The magnetic swarming motion will decrease the use of surfactants and peroxide fuel for propulsion and greatly enhance the catalytic degradation performance. Thus, the magnetic mode of degradation by FMO micromotors will improve the practical application potential.

Besides the heat-treatment process in air, we also tried to tailor the morphology and phase composition of iron-manganese oxides micromotors in N_2 atmosphere. Fig. S10–S11 shows the SEM images and XRD patterns of the FMO micromotors after heat-treatment at 400 °C for 10 min in N_2 atmosphere. Amorphous MnO_2 decomposed to a Mn_3O_4 phase. Besides, the reaction of MnO_2 with pure iron also formed an oxide

of $(\text{FeO})_{0.664}(\text{MnO})_{0.336}$ in a tiny quantity. SEM images show that most of the original flower-like nanoplates transformed into rough convex dot-like decorations on the surface. Optical observation of the movement of these particles demonstrates their low mobility in 5% H_2O_2 fuel. Hence, given their phase composition and motion behaviors, N_2 atmosphere calcination is not a good choice for improving mobility, and we focused on hydrothermally synthesized and air heat-treated samples for movement and decontamination tests. FMO and FMO300 contain the birnessite MnO_2 shell and iron core, while the quantity of surface MnO_2 nanoplates on FMO300 was lower than on FMO. FMO400 micromotors have a certain degree of oxidation compared with FMO and FMO300 micromotors. FMO450 has α - MnO_2 and Fe_3O_4 phases due to the higher temperature oxidation.

3.2. FMO micromotors' movements and magnetic manipulations

Fig. 4 presents the mobility performances of FMO micromotors. The time-lapse images were extracted from the supporting information

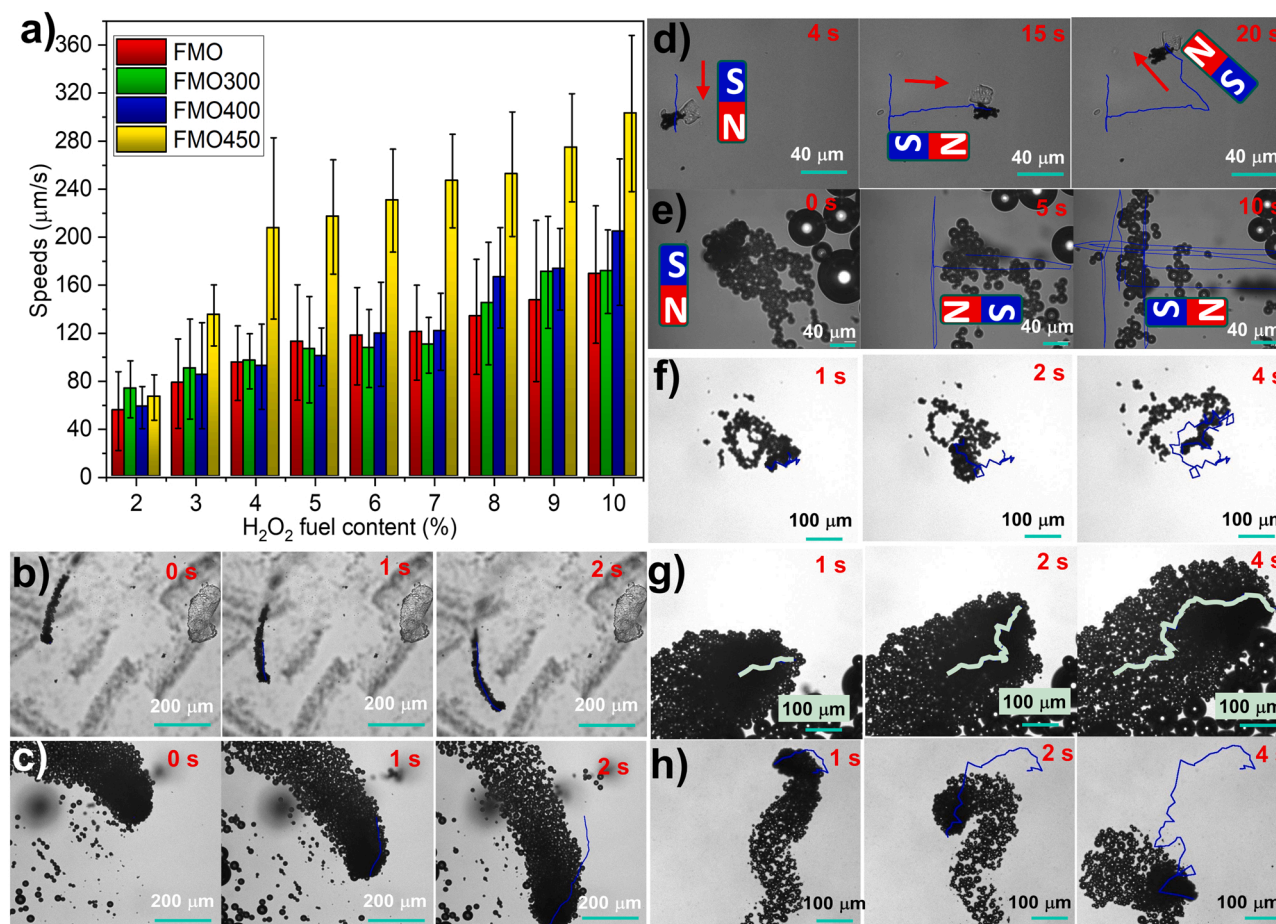


Fig. 4. FMO micromotors' movement behaviors. (a) Average speeds of micromotors are dependent on the varying peroxide content. Error bars were obtained from 50 observations. Captured images depict the motion behaviors. (b) FMO micromotors in 2% H₂O₂; (c) FMO micromotor's self-propelling motion in 10% H₂O₂; (d) Magnetic steering of an FMO micromotor to move; (e) Magnetic steering of an FMO micromotor in 5% H₂O₂. (f) Bubble propelling of an FMO300 micromotor in 8% of H₂O₂; (g) Bubble propelling of an FMO400 micromotor in 6% H₂O₂; (h) Self-propelling of an FMO450 micromotor in 9% H₂O₂. 0.5% SDS as the surfactant.

videos S1-S7. These iron-manganese oxide micromotors demonstrate good motion behaviors from as low as 2% peroxide fuel solutions. The bubbles propelled motion behaviors were operated using 0.5% SDS as the surfactant to lower interfacial free energy and facilitate bubble formation and detachment for propulsion. Fig. 4a shows the average speeds at different H₂O₂ contents. All these iron-manganese oxides motors demonstrate good mobility. As the peroxide fuel content increases, the average speed of motors increases dramatically. As shown by the SEM images, the hydrothermally fabricated FMO micromotors have the worst asymmetry. Flower-like MnO₂ nanoplates cover the iron core uniformly, and the core-shell particles are round with an average diameter of a few micrometers. The FMO micromotors' speed increased from 55.2 ± 32.9 μm/s in 2% H₂O₂ fuel to 168.9 ± 57.2 μm/s in 10% H₂O₂ fuel. As the higher fuel content results in higher bubble generation rates, a more significant propulsion force is exerted on the micromotors. After heat-treatment, parts of MnO₂ nanoplates were exfoliated, resulting in a higher degree of asymmetry. The XRD data demonstrates that no phase transition occurred at the heating temperature of 300 °C. At 2% H₂O₂, FMO300 increased its speed by 41% to 78.1 ± 37.2 μm/s, compared with the as-hydrothermally synthesized FMO micromotors. The calcination-induced asymmetry increased the mobility of micromotors. The speed of FMO300 micromotors increased to 171.3 ± 34.8 μm/s in 10% peroxide fuel.

Supplementary material related to this article can be found online at [doi:10.1016/j.apcatb.2022.121484](https://doi.org/10.1016/j.apcatb.2022.121484).

FMO400 micromotors show significantly faster speeds at high fuel contents, and the speed increases from 58.1 ± 17.7 – 204.3 ± 61 μm/s at

2–10% peroxide. The higher speeds were due to a higher degree of asymmetry. Besides, a higher degree of exfoliation at 400 °C may reduce the size of the core-shell motors as more surface MnO₂ nanoplates were exfoliated by high temperatures. Thus, the fluid resistance is reduced to a marked degree.

FMO450 micromotors show a dramatic speed increase (Fig. 4a). The excellent mobility was due to a phase transition to α-MnO₂, which has a much higher catalytic activity towards peroxide decomposition. The speed of FMO450 micromotors is 66.5 ± 19 μm/s in 2% H₂O₂ fuel, while it increased to over 200 μm/s in 4% peroxide fuel, faster than the speeds of FMO, FMO300, and FMO400 micromotors in 10% peroxide fuel. The speeding tendency agrees with previous results, as the phase transition induced speed increases was due to the higher catalytic activity by α-MnO₂ [9]. The heat-treatment to induce a phase transition of MnO₂ can be a powerful method to enhance mobility and lower the peroxide fuel content for MnO₂ based bubble propelling motors. FMO450 micromotors can have a speed of over 300 μm/s as the peroxide fuel content gradually increases to 10%.

Fig. 4b-c shows the time-lapse images of FMO micromotors in 2% and 10% peroxide fuel. Due to the large density of the iron core, small propelling force, and weak bubbling process, these small heavy propellers tend to sink to the bottom of motion observation container. At a higher fuel content, a fast-bubbling process would uplift the motors to a floating state. Fig. 4d shows an FMO micromotor's steering by an external magnetic field to move a small particle. Fig. 4e shows the magnetic steering of bubble propelling micromotors. The magnetic forces exerted on the FMO micromotors are significantly larger than our

previously developed micromotors [9]. The blue trajectory of the bubble driving micromotors in Fig. 4e shows that the magnetic forces are powerful, as the micromotor moved a long distance swiftly. It quickly moved out of the microscope view.

Fig. 4f presents the time-lapse images of FMO300 micromotors in a random movement in 8% peroxide fuel. After the calcination, the higher degree of asymmetry improved the movement. Fig. 4g and h show the typical time-lapse motion images of FMO400 and FMO450 micromotors. From the above analysis, calcination induced a higher asymmetry degree. The phase transition of MnO_2 significantly improved the movement of the as-synthesized Fe- MnO_2 catalytic motors.

3.3. FMO micromotors for TC decontamination

Previously, Lee et al. designed Fe-Pt Janus motors for organic degradation [32]. The reliance on Pt as the catalytic engine for motion inevitably refused practical applications of these motors. Besides, the mobility is still not very good. Hence, we combined the highly efficient Fenton reaction-based remediation with MnO_2 based micro-/nanomotors. Fig. S12 presents the linear fit of the TC content with the absorbance data up to 100 mg/L TC. Fig. 5a shows TC decontamination

in the presence of surfactant and motors. Without the catalytic motors, a minimal removal occurs due to the natural decomposition of H_2O_2 to generate reactive radicals. The solution with the surfactant shows even less degradation as the surfactant shields the antibiotic molecules in the solution. After introducing catalytic FMO motors into the reaction solution, significant degradation takes place in a short time. Triton-X-100 surfactant at 0.01% also protected the antibiotic pollutants from the attack by reactive radicals. The surfactant is quite indispensable for the bubble propelled motors to move. The generation of large quantities of bubbles may provide other advantages by the adsorptive bubble separation (ABS) mechanism [45]. Previously, researchers demonstrated the ABS for dissolvable dyes [46]. Very recently, we demonstrated the role of ABS in suspended microplastic pollutant removal [9]. The ABS mechanism could separate at least 10% of microplastics. While to our knowledge, the motors-assisted ABS for antibiotics decontamination has not been demonstrated.

Fig. 5a shows that the ABS and catalytic degradation could remove nearly 75% of the antibiotics, and more than 80% removal was achieved without the surfactant in 2-h. The good remediation performance was attributed to the synergy of the Fenton reaction and MnO_2 based Fenton-like reactions. Fig. S13 shows the photograph of reaction solutions with

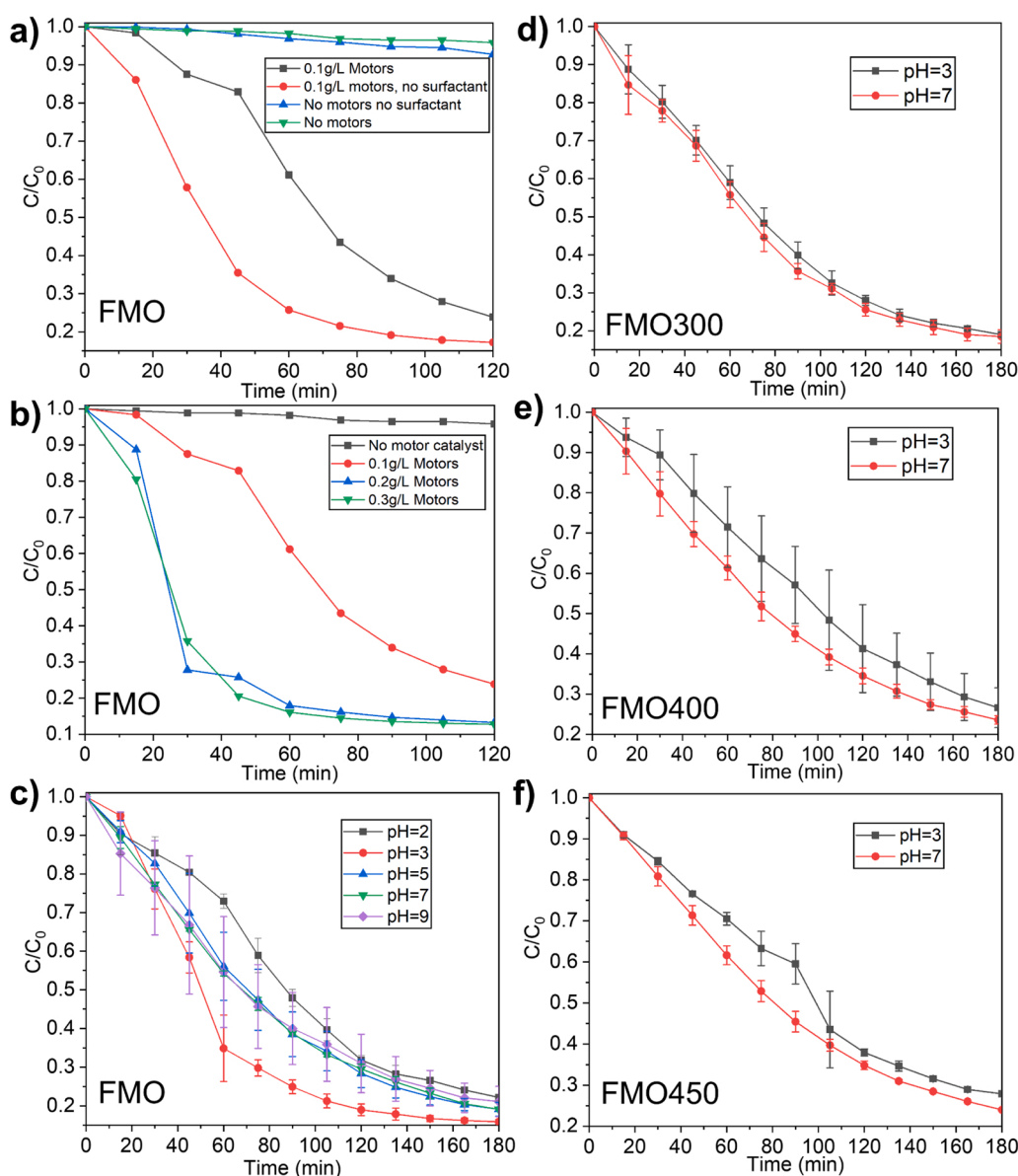


Fig. 5. FMO micromotors' TC removal performances: (a) Surfactant and FMO micromotors on the decontamination performance. Initial pH = 3. (b) Effect of the dosage of FMO core-shell micromotors on TC removal for 2-h reaction time. Initial condition: pH = 3. (c) Effect of the pH conditions on decontamination for 3-h reaction time with 0.1 g/L FMO motors as the catalyst. Decontamination of TC by the heat-treated iron-manganese oxides core-shell micromotors under acidic (pH = 3) and neutral (pH = 7) condition: (d) FMO300, (e) FMO400, and (f) FMO450. Error bars were obtained from 3 observations. Experimental conditions: 0.01% Triton-X-100, 50 mg/L of TC, 5% H_2O_2 as a fuel and oxidant.

a load of 0.1 g/L catalysts. The height of the generated foam reflects the bubble generation. At pH = 3, considerable microbubbles were developed in the first 20 min. Then more bubbles broke up rather than developed, resulting in a foam phase reduction. Hence, we can infer that the reactive radicals mainly contributed to the decontamination at 0.1 g/L catalysts of pH = 3 by the Fenton and Fenton-like reactions.

Fig. 5b shows the influence of the motor dosage on the decontamination performance at pH = 3. A higher catalytic motor dosage significantly improves the decontamination performance. In just 1-h reaction time, the decontamination reached about 85% by the FMO micromotors with 0.2 and 0.3 g/L motor dosage. Fig. S14–15 shows the photographs of the corresponding degradation process with 0.2 and 0.3 g/L catalytic motors. Significantly more foam was generated with the help of more catalytic motor dosage. Thus, the ABS plays a crucial role in the decontamination process, especially at the beginning of half an hour. In 15 min reaction time, the catalytic motors at 0.3 g/L result in slightly higher decontamination performance than that at 0.2 g/L. The corresponding photograph shows that more catalytic motors in this period result in significantly more bubble generation. As the photographs show, the foam height in the reaction vessel at 0.3 g/L is much higher than that in the case of 0.2 g/L. Prolonging the reaction time to 30 min, we observed the opposite results. The foam height of reaction solution at 0.2 g/L in 32 min is much higher than that in 0.3 g/L reaction solution at 25–34 min. The photographs are in good agreement with the degradation curves in Fig. 5b that 30 min reaction time results in slightly higher decontamination for the system of 0.2 g/L than 0.3 g/L. Thus, we clarified the importance of the ABS mechanism in the TC antibiotic removal. With more motors added, higher separation rates were achieved at the beginning. The results are similar to our previous report on dye removal [9].

Here, catalytic degradation also plays an essential role in the overall decontamination process. We observed the reduction of foam phase as time went by, while the decontamination curves showed decreasing tendency continuously. The high ROS would continuously attack the dissolved antibiotics, contributing to the overall decontamination performance. Due to the competing effect of ABS and catalytic degradation mechanisms, the overall decontamination performances at 0.2 and 0.3 g/L catalytic motors show a reasonably equivalent outcome. Although a high dosage of catalytic motors results in better ABS initially, more overall catalytic degradations compensated for the less adsorptive removals by bubbles for the lower dosage of 0.2 g/L motors. Thus, both reactions reached identical decontamination of over 85% antibiotic removals from the polluted water after 2-h. In 1-h reaction time, both reactions degraded over 80% of pollutants, which is comparable to the previous work by Maria-Hormigos et al. The carbon nanotubes-ferrite-manganese dioxide tubular micromotors removed 80% of 4-chlorophenol in 1-h [23]. Despite the different contaminants, we only used 0.2–0.3 g/L of FMO core-shell micromotors, much lower than 4 g/L of tubular micromotors to achieve the same removal percentage, suggesting high performance of the newly developed core-shell micromotors.

Fig. 5c shows the influence of pH values on TC decontamination. The alkaline environment promotes MnO_2 's activity for H_2O_2 decomposition. Thus, the decontamination performance was usually higher for the MnO_2 based MNMs at higher pH values [46]. It is well known that the iron-containing Fenton reaction has the optimal pH value range of 2–4 [33]. FMO micromotors contain two types of catalysts. Besides, the ABS mechanism also contributes to the overall decontamination. Hence, we performed the antibiotic decontamination tests by FMO micromotors for a pH range from 2 to 9. It seems that pH = 3 generates the best overall decontamination process as the Fenton reaction is the major contributor to the decontamination of TC. In comparison, the worst decontamination performance occurs at pH 2, as both the Fenton reaction and MnO_2 based decontamination processes were depressed to a great extent due to the high acidity.

At pH 5–9, FMO micromotors show similar decontamination performance. The higher alkalinity of solutions resulted in a higher bubble

separation process and improved MnO_2 based decontaminations, although the Fenton reaction were depressed. The results are in good agreement with the photographs in Fig. S13 right-side images. At pH 7, the reaction generates significantly more bubbles in the process. Thus, for the original FMO core-shell micromotors without heat treatment, the optimal decontamination pH value is 3, and after 3-h reaction time, nearly 90% of the antibiotic was removed. At pH 2 and 5–9, the FMO micromotors still achieved 75–80% of the decontamination, suggesting these smart core-shell micromotors demonstrate excellent performance for TC elimination.

To evaluate the decontamination performances of heat-treated FMO micromotors for TC removal, we tested FMO300, FMO400, and FMO450 micromotors in the optimal pH value of 3 and neutral conditions. Fig. 5d–f shows the TC decontamination profiles by the three micromotors. Fig. S16–18 presents the corresponding photographs of degradation process. FMO300 micromotors show a slight improvement in decontamination performance at neutral conditions compared with that at acidic pH 3. The results are different from the untreated FMO micromotors. In the acidic condition, FMO micromotors show better decontamination owing to higher radical oxidation from the Fenton reaction. The XRD patterns show that no iron oxide phases formed in the FMO300 micromotors. The zero-valence iron-based catalyst has a higher catalytic activity than the iron oxides-based catalyst [47]. The higher degree of the calcination process, the more oxidation layer formed on the iron cores. Thus, the Fenton reaction was depressed. FMO300 micromotors could decompose more than 80% of the antibiotics in 3-h and about 75% in 2-h reaction time, demonstrating its excellent potential for antibiotics removals. Fig. S16 shows that the reaction in the neutral conditions generates slightly more microbubbles and foam than acidic ones. Thus, the ABS mechanism may contribute to the higher decontamination performance in neutral than in acidic conditions. The combined effect of catalytic degradation by Fenton/Fenton-like reactions and adsorption separation by micro bubbles improved the overall decontamination performance. We believe that a wide range of organics, microorganisms, and suspended particle pollutants could be removed by the multiple mechanisms with enhanced efficiency.

Fig. 5e–f shows a similar tendency as Fig. 5d that the neutral condition has a better remediation performance than the acidic conditions for the heat-treated iron-manganese oxides micromotors. The reason for the weaker decontamination of TC in an acidic environment should be attributed to the oxidation of iron core catalysts. In about 3-h reaction time, all the heat-treated FMO micromotors achieved 70%–80% removals, demonstrating good antibiotic removal capability in a wide pH range from 2 to 7. Fig. S19 shows the decontamination profiles of TC by the four iron-manganese oxides micromotors. At a pH value of 3, the decontamination performances of these iron-manganese oxides micromotors are in the following order: FMO > FMO300 > FMO400 ≈ FMO450. Under a neutral environment, their environmental cleaning activity follows FMO300 > FMO > FMO400 ≈ FMO450.

We then tested the generation of reactive species using FMO and FMO400 micromotors in acidic and neutral conditions by EPR. Fig. 6 and Fig. S20 show the EPR spectra from FMO and FMO400 micromotors, respectively. Fig. 6a shows that, after the addition of FMO micromotors, significant $\cdot\text{OH}$ and atomic H^{\cdot} reactive species were generated in the neutral condition. Fig. 6b and d show that FMO micromotors also generate large quantities of $^1\text{O}_2$ in neutral and acidic conditions. Fig. 6c shows a large quantity of $\cdot\text{OH}$ and a small quantity of atomic H^{\cdot} were generated in the optimal pH value of 3. To the best of our knowledge, the atomic H^{\cdot} reactive species were rarely detected by EPR techniques with the Fenton or Fenton-like environmental decontaminations [48]. Makino et al. discovered the co-existence of $\cdot\text{OH}$ and atomic H^{\cdot} in the sonolysis of water solution with DMPO as the spin trapping agent; no one has ever identified the atomic H^{\cdot} reactive species in synthetic motors assisted decontamination process [49]. To our surprise, a small portion of DMPO- CH_3 or DMPO- CH_2OH adjunct was also detected. It can be inferred that the large quantity of highly reactive $\cdot\text{OH}$ has already

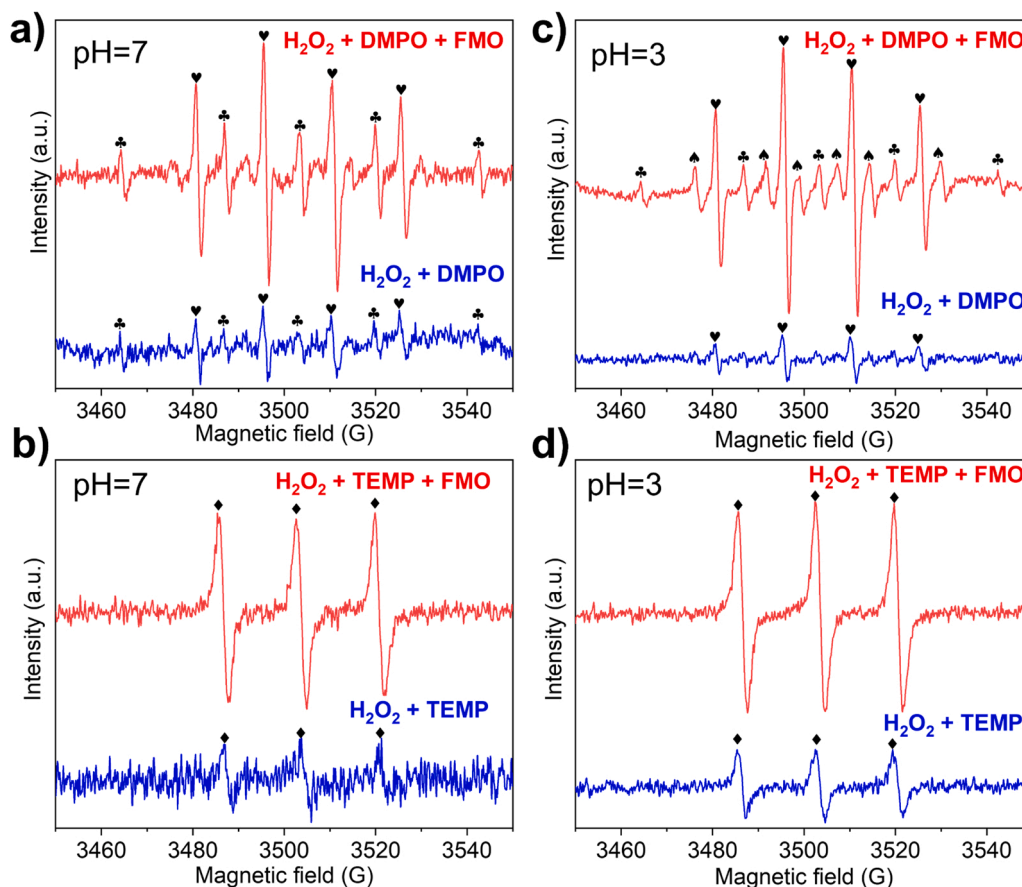


Fig. 6. EPR spectra of H_2O_2 activation by FMO micromotors: (a) DMPO as the trapping agents at pH = 7; (b) TEMP as the trapping agents at pH = 7; (c) DMPO as the trapping agents at pH = 3; (d) TEMP as the trapping agents at pH = 3. FMO catalyst, 0.3 g/L; H_2O_2 , 2.5%; temperature, 25 °C; DMPO, 0.08 M; TEMP, 0.08 M; ♥, DMPO-OH; ♣, DMPO-CH₃ or DMPO-CH₂OH; ♠, DMPO-H; ♦, TEMP- $^1\text{O}_2$.

decomposed a portion of the DMPO compound to generate the organic radicals, $\cdot\text{CH}_3$ or $\cdot\text{CH}_2\text{OH}$. These two radicals have similar EPR patterns. Under the higher pH value of 7, more amount of atomic H^* reactive species was generated. As previously demonstrated by Qu et al., the atomic H^* would react with peroxide to generate H_2O and $\cdot\text{OH}$, thus extending the pH range to neutral conditions with high decontamination performance [35].

Fig. S20a shows that even more atomic H^* reactive species were generated in neutral conditions for FMO400 micromotors, while in acidic conditions, more $\cdot\text{OH}$ was generated than in the neutral condition. As the atomic H^* reactive species react with peroxide to generate $\cdot\text{OH}$ continuously, FMO400 micromotors show better decontamination performances in neutral conditions than in acidic pH 3. We believe that the synergistic effect of atomic H^* with $\cdot\text{OH}$ by FMO400 micromotors in peroxide solutions at neutral pH exceeded that at pH 3. Heat-treated FMO micromotors generate much more atomic H^* species in the neutral condition, which would react with peroxide to produce $\cdot\text{OH}$ for enhanced degradation. Besides, the singlet oxygen also participates in the decontamination processes for all the motors systems at varied pH conditions. Based on previous studies, $\text{O}_2^{\cdot-}$ was the dominant ROS in the MnO_2 - H_2O_2 systems at neutral pH [50]. He et al. demonstrated that $\text{O}_2^{\cdot-}$ and $\cdot\text{OH}$ could be generated synchronously by activating H_2O_2 with a MnO_2 catalyst [51]. However, the superoxide radicals were not detected in this work.

We also used the PL method to identify $\cdot\text{OH}$ in the degradation process. We used the terephthalic acid as the probe molecule to react with the generated $\cdot\text{OH}$ to form 2-hydroxyterephthalic acid, a fluorescent molecule [52]. Fig. S21 shows the relation between the $\cdot\text{OH}$ generation and reaction time. Before adding the micromotors to the solution, the

hydroxyl radicals were produced from the self-decomposition of H_2O_2 . After adding the FMO micromotors, the reaction solution generated significantly more $\cdot\text{OH}$ radicals. The red curve of fluorescence spectra shows more $\cdot\text{OH}$ generation in 15 min. As time goes by, a higher intensity of spectrum peaks could be obtained due to the good catalytic activity by the FMO catalyst to generate $\cdot\text{OH}$. The results further confirmed the generation of $\cdot\text{OH}$ in the H_2O_2 /FMO system as the leading oxidative radicals.

4. Conclusions

We fabricated low-cost iron-manganese oxides-based micromotors by a simple hydrothermal reaction and heat-treatment method using inexpensive synthetic materials in a scalable production with superior decontamination performance for antibiotics. The morphology, mobility, and antibiotic contaminant removal of the iron-manganese oxides core-shell micromotors were investigated. Thermal exfoliation of surface MnO_2 nanoplates increased the asymmetry and mobility of these core-shell propellers. The micromotors show magnetic steering ability, and quick bubble propelled motion from 2% H_2O_2 fuel with a high speed of over 300 $\mu\text{m/s}$ in 10% peroxide fuel. Higher temperature calcination results in the formation of an iron oxide phase, shielding the iron-core reaction with peroxide fuel to generate reactive radicals and decreasing the decontamination performance slightly. The reactive species for the fast decontamination of TC antibiotics were also identified. Atomic H^* mediated $\cdot\text{OH}$ generation extends the pH range of acidic conditions to neutral with high catalytic degradation performance. The calcined FMO micromotors show better removal efficiencies in neutral conditions. The synergy of ABS and catalytic degradation by iron and

manganese oxides of the FMO micromotors demonstrate highly efficient and fast decontamination in a wide pH range, making them a great alternative to previously developed Pt-based motors for practical environmental cleaning purposes. This work may profoundly impact other research fields, such as chemosynthesis, tumor therapy, and protein modification.

CRedit authorship contribution statement

Heng Ye: Conceptualization, Methodology, Investigation, Formal analysis, Validation, Visualization, Writing – original draft. **Shengnan Wang:** Methodology, Investigation. **Yong Wang:** Investigation, Methodology. **Peiting Guo:** Investigation, Methodology. **Liying Wang:** Investigation, Methodology. **Chengke Zhao:** Methodology, Investigation. **Shuqing Chen:** Investigation, Methodology. **Yimai Chen:** Methodology, Investigation. **Hongqi Sun:** Conceptualization, Writing – review & editing, Funding acquisition. **Shaobin Wang:** Conceptualization, Writing – review & editing, Funding acquisition. **Xing Ma:** Conceptualization, Writing – review & editing, Supervision, Resources, Project administration, Funding acquisition.

Declaration of Competing Interest

The authors declare that they have no known competing financial interests or personal relationships that could have appeared to influence the work reported in this paper.

Acknowledgments

The authors thank the financial support from Shenzhen Bay Laboratory (SZBL2019062801005), Shenzhen Science and Technology Program (KQTD20170809110344233), Natural Science Foundation of Guangdong Province (No. 2019A151010762), and the National Natural Science Foundation of China (51802060), as well as the Australian Research Council (DP190103548). The authors thank the insightful discussion with Dr. Ping Liang from Wuyi University. We would also like to express our thanks to Lulu Zhao from the School of Science of Harbin Institute of Technology (Shenzhen) for her assistance in EPR testing.

Appendix A. Supporting information

Supplementary data associated with this article can be found in the online version at [doi:10.1016/j.apcatb.2022.121484](https://doi.org/10.1016/j.apcatb.2022.121484).

References

- [1] Y. Wang, W. Duan, C. Zhou, Q. Liu, J. Gu, H. Ye, M. Li, W. Wang, X. Ma, Phoretic liquid metal micro/nanomotors as intelligent filler for targeted microwelding, *Adv. Mater.* 31 (2019), e1905067, <https://doi.org/10.1002/adma.201905067>.
- [2] H. Ye, Y. Wang, D. Xu, X. Liu, X. Ma, Design and fabrication of micro/nanomotors for environmental and sensing applications, *Appl. Mater. Today* 23 (2021), 101007, <https://doi.org/10.1016/j.apmt.2021.101007>.
- [3] H. Zhou, C.C. Mayorga-Martinez, S. Pane, L. Zhang, M. Pumera, Magnetically driven micro and nanorobots, *Chem. Rev.* 121 (2021) 4999–5041, <https://doi.org/10.1021/acs.chemrev.0c01234>.
- [4] M. Safdar, S.U. Khan, J. Janis, Progress toward catalytic micro- and nanomotors for biomedical and environmental applications, *Adv. Mater.* 30 (2018), e1703660, <https://doi.org/10.1002/adma.201703660>.
- [5] L. Soler, V. Magdanz, V.M. Fomin, S. Sanchez, O.G. Schmidt, Self-propelled micromotors for cleaning polluted water, *ACS Nano* 7 (2013) 9611–9620, <https://doi.org/10.1021/nn405075d>.
- [6] F.Z. Mou, D. Pan, C.R. Chen, Y.R. Gao, L.L. Xu, J.G. Guan, Magnetically modulated pot-like MnFe_2O_4 micromotors: Nanoparticle assembly fabrication and their capability for direct oil removal, *Adv. Funct. Mater.* 25 (2015) 6173–6181, <https://doi.org/10.1002/adfm.201502835>.
- [7] H. Wang, B. Khezri, M. Pumera, Catalytic DNA-functionalized self-propelled micromachines for environmental remediation, *Chem* 1 (2016) 473–481, <https://doi.org/10.1016/j.chempr.2016.08.009>.
- [8] M. Hoop, Y. Shen, X.Z. Chen, F. Mushtaq, L.M. Iuliano, M.S. Sakar, A. Petruska, M. J. Loessner, B.J. Nelson, S. Pane, Magnetically driven silver-coated nanocoils for efficient bacterial contact killing, *Adv. Funct. Mater.* 26 (2016) 1063–1069, <https://doi.org/10.1002/adfm.201504463>.
- [9] H. Ye, Y. Wang, X. Liu, D. Xu, H. Yuan, H. Sun, S. Wang, X. Ma, Magnetically steerable iron oxides-manganese dioxide core-shell micromotors for organic and microplastic removals, *J. Colloid Interface Sci.* 588 (2021) 510–521, <https://doi.org/10.1016/j.jcis.2020.12.097>.
- [10] W.F. Paxton, P.T. Baker, T.R. Kline, Y. Wang, T.E. Mallouk, A. Sen, Catalytically induced electrokinetics for motors and micropumps, *J. Am. Chem. Soc.* 128 (2006) 14881–14888, <https://doi.org/10.1021/ja0643164>.
- [11] W. Wang, W.T. Duan, S. Ahmed, T.E. Mallouk, A. Sen, Small power: autonomous nano- and micromotors propelled by self-generated gradients, *Nano Today* 8 (2013) 531–554, <https://doi.org/10.1016/j.nantod.2013.08.009>.
- [12] H. Ye, G. Ma, J. Kang, H. Sun, S. Wang, Pt-free microengines at extremely low peroxide levels, *Chem. Commun.* 54 (2018) 4653–4656, <https://doi.org/10.1039/c8cc01548a>.
- [13] L. Zhang, J.J. Abbott, L. Dong, K.E. Peyer, B.E. Kratochvil, H. Zhang, C. Bergeles, B. J. Nelson, Characterizing the swimming properties of artificial bacterial flagella, *Nano Lett.* 9 (2009) 3663–3667, <https://doi.org/10.1021/nl901869j>.
- [14] Y. Dong, C. Yi, S. Yang, J. Wang, P. Chen, X. Liu, W. Du, S. Wang, B.F. Liu, A substrate-free graphene oxide-based micromotor for rapid adsorption of antibiotics, *Nanoscale* 11 (2019) 4562–4570, <https://doi.org/10.1039/c8nr09229j>.
- [15] H. Wang, G. Zhao, M. Pumera, Blood electrolytes exhibit a strong influence on the mobility of artificial catalytic microengines, *Phys. Chem. Chem. Phys.* 15 (2013) 17277–17280, <https://doi.org/10.1039/c3cp52726c>.
- [16] K. Villa, J. Parmar, D. Vilela, S. Sanchez, Metal-oxide-based microjets for the simultaneous removal of organic pollutants and heavy metals, *ACS Appl. Mater. Interfaces* 10 (2018) 20478–20486, <https://doi.org/10.1021/acsmi.8b04353>.
- [17] W. Ma, K. Wang, S. Pan, H. Wang, Iron-exchanged zeolite micromotors for enhanced degradation of organic pollutants, *Langmuir* 36 (2020) 6924–6929, <https://doi.org/10.1021/acs.langmuir.9b02137>.
- [18] H. Shi, X. Chen, K. Liu, X. Ding, W. Liu, M. Xu, Heterogeneous Fenton ferroferric oxide-reduced graphene oxide-based composite microjets for efficient organic dye degradation, *J. Colloid Interface Sci.* 572 (2020) 39–47, <https://doi.org/10.1016/j.jcis.2020.03.073>.
- [19] W. Liu, H. Ge, X. Ding, X. Lu, Y. Zhang, Z. Gu, Cubic nano-silver-decorated manganese dioxide micromotors: enhanced propulsion and antibacterial performance, *Nanoscale* 12 (2020) 19655–19664, <https://doi.org/10.1039/d0nr06281b>.
- [20] J. Parmar, K. Villa, D. Vilela, S. Sanchez, Platinum-free cobalt ferrite based micromotors for antibiotic removal, *Appl. Mater. Today* 9 (2017) 605–611, <https://doi.org/10.1016/j.apmt.2017.11.002>.
- [21] J. Liu, J. Li, G. Wang, W. Yang, J. Yang, Y. Liu, Bioinspired zeolitic imidazolate framework (ZIF-8) magnetic micromotors for highly efficient removal of organic pollutants from water, *J. Colloid Interface Sci.* 555 (2019) 234–244, <https://doi.org/10.1016/j.jcis.2019.07.059>.
- [22] X. He, R. Buchel, R. Figi, Y. Zhang, Y. Bahk, J. Ma, J. Wang, High-performance carbon/MnO₂ micromotors and their applications for pollutant removal, *Chemosphere* 219 (2019) 427–435, <https://doi.org/10.1016/j.chemosphere.2018.12.051>.
- [23] R. Maria-Hormigos, M. Pacheco, B. Jurado-Sanchez, A. Escarpa, Carbon nanotubes-ferrite-manganese dioxide micromotors for advanced oxidation processes in water treatment, *Environ. Sci. Nano* 5 (2018) 2993–3003, <https://doi.org/10.1039/c8en00824h>.
- [24] H. Wang, T. Chen, D. Chen, X. Zou, M. Li, F. Huang, F. Sun, C. Wang, D. Shu, H. Liu, Sulfurized oolitic hematite as a heterogeneous Fenton-like catalyst for tetracycline antibiotic degradation, *Appl. Catal. B* 260 (2020), 118203, <https://doi.org/10.1016/j.apcatb.2019.118203>.
- [25] B. Zhang, S. Wang, Y. Li, P. Sun, C. Yang, D. Wang, L. Liu, Review: phase transition mechanism and supercritical hydrothermal synthesis of nano lithium iron phosphate, *Ceram. Int.* 46 (2020) 27922–27939, <https://doi.org/10.1016/j.ceramint.2020.08.105>.
- [26] K. Sekar, C. Chuaicham, B. Vellaichamy, W. Li, W. Zhuang, X. Lu, B. Ohtani, K. Sasaki, Cubic Cu₂O nanoparticles decorated on TiO₂ nanofiber heterostructure as an excellent synergistic photocatalyst for H₂ production and sulfamethoxazole degradation, *Appl. Catal. B* 294 (2021), 120221, <https://doi.org/10.1016/j.apcatb.2021.120221>.
- [27] J. Wang, R. Zhuan, Degradation of antibiotics by advanced oxidation processes: an overview, *Sci. Total Environ.* 701 (2020), 135023, <https://doi.org/10.1016/j.scitotenv.2019.135023>.
- [28] X. Nie, G. Li, S. Li, Y. Luo, W. Luo, Q. Wan, T. An, Highly efficient adsorption and catalytic degradation of ciprofloxacin by a novel heterogeneous Fenton catalyst of hexapod-like pyrite nanosheets mineral clusters, *Appl. Catal. B* 300 (2022), 120734, <https://doi.org/10.1016/j.apcatb.2021.120734>.
- [29] P. Ding, H. Ji, P. Li, Q. Liu, Y. Wu, M. Guo, Z. Zhou, S. Gao, W. Xu, W. Liu, Q. Wang, S. Chen, Visible-light degradation of antibiotics catalyzed by titania/zirconia/graphitic carbon nitride ternary nanocomposites: a combined experimental and theoretical study, *Appl. Catal. B* 300 (2022), 120633, <https://doi.org/10.1016/j.apcatb.2021.120633>.
- [30] D. Xing, Z. Cui, Y. Liu, Z. Wang, P. Wang, Z. Zheng, H. Cheng, Y. Dai, B. Huang, Two-dimensional π -d conjugated metal-organic framework Fe₃(hexaiminotriphenylene)₂ as a photo-Fenton like catalyst for highly efficient degradation of antibiotics, *Appl. Catal. B* 290 (2021), 120029, <https://doi.org/10.1016/j.apcatb.2021.120029>.
- [31] P. Liang, C. Zhang, X. Duan, H. Sun, S. Liu, M.O. Tade, S. Wang, N-doped graphene from metal-organic frameworks for catalytic oxidation of p-hydroxybenzoic acid: N-functionality and mechanism, *ACS Sustain. Chem. Eng.* 5 (2017) 2693–2701, <https://doi.org/10.1021/acssuschemeng.6b03035>.

- [32] C.S. Lee, J.Y. Gong, D.S. Oh, J.R. Jeon, Y.S. Chang, Zerovalent-iron/platinum Janus micromotors with spatially separated functionalities for efficient water decontamination, *ACS Appl. Nano Mater.* 1 (2018) 768–776, <https://doi.org/10.1021/acsanm.7b00223>.
- [33] S. Wang, A Comparative study of Fenton and Fenton-like reaction kinetics in decolourisation of wastewater, *Dyes Pigm.* 76 (2008) 714–720, <https://doi.org/10.1016/j.dyepig.2007.01.012>.
- [34] X.J. Yang, X.M. Xu, J. Xu, Y.F. Han, Iron oxychloride (FeOCl): an efficient Fenton-like catalyst for producing hydroxyl radicals in degradation of organic contaminants, *J. Am. Chem. Soc.* 135 (2013) 16058–16061, <https://doi.org/10.1021/ja409130c>.
- [35] H. Zeng, G. Zhang, Q. Ji, H. Liu, X. Hua, H. Xia, M. Sillanpää, J. Qu, pH-independent production of hydroxyl radical from atomic H[•]-mediated electrocatalytic H₂O₂ reduction: A green Fenton process without byproducts, *Environ. Sci. Technol.* 54 (2020) 14725–14731, <https://doi.org/10.1021/acs.est.0c04694>.
- [36] Z. Li, X. Qin, Z. Zhu, S. Zheng, H. Li, H. Fu, H. Zhang, Cu-based metallic glass with robust activity and sustainability for wastewater treatment, *J. Mater. Chem. A* 8 (2020) 10855–10864, <https://doi.org/10.1039/D0TA01693D>.
- [37] W. Liu, H. Ge, X. Chen, X. Lu, Z. Gu, J. Li, J. Wang, Fish-scale-like intercalated metal oxide-based micromotors as efficient water remediation agents, *ACS Appl. Mater. Interfaces* 11 (2019) 16164–16173, <https://doi.org/10.1021/acsami.9b01095>.
- [38] H. Ye, H.Q. Sun, S.B. Wang, Electrochemical synthesis of graphene/MnO₂ in an architecture of bilayer microtubes as micromotors, *Chem. Eng. J.* 324 (2017) 251–258, <https://doi.org/10.1016/j.cej.2017.05.036>.
- [39] Y. Yao, H. Hu, H. Yin, M. Yu, H. Zheng, Y. Zhang, S. Wang, Phase change on stainless-steel mesh for promoting sulfate radical formation via peroxymonosulfate oxidation, *Appl. Catal. B* 278 (2020), 119333, <https://doi.org/10.1016/j.apcatb.2020.119333>.
- [40] L. Zhang, L. Qiu, Q. Zhu, X. Liang, J. Huang, M. Yang, Z. Zhang, J. Ma, J. Shen, Insight into efficient degradation of 3,5-dichlorosalicylic acid by Fe-Si-B amorphous ribbon under neutral condition, *Appl. Catal. B* 294 (2021), 120258, <https://doi.org/10.1016/j.apcatb.2021.120258>.
- [41] R. Yang, Y. Fan, R. Ye, Y. Tang, X. Cao, Z. Yin, Z. Zeng, MnO₂-based materials for environmental applications, *Adv. Mater.* 33 (2021), e2004862, <https://doi.org/10.1002/adma.202004862>.
- [42] M. Safdar, O.M. Wani, J. Janis, Manganese oxide-based chemically powered micromotors, *ACS Appl. Mater. Inter.* 7 (2015) 25580–25585, <https://doi.org/10.1021/acsami.5b08789>.
- [43] L.B. Song, C.Q. Li, W. Chen, B. Liu, Y.D. Zhao, Highly efficient MnO₂/reduced graphene oxide hydrogel motors for organic pollutants removal, *J. Mater. Sci.* 55 (2020) 1984–1995, <https://doi.org/10.1007/s10853-019-04076-5>.
- [44] Y. Wang, H. Sun, H.M. Ang, M.O. Tade, S. Wang, Facile synthesis of hierarchically structured magnetic MnO₂/ZnFe₂O₄ hybrid materials and their performance in heterogeneous activation of peroxymonosulfate, *ACS Appl. Mater. Interfaces* 6 (2014) 19914–19923, <https://doi.org/10.1021/am505309b>.
- [45] O.M. Wani, M. Safdar, N. Kinnunen, J. Janis, Dual effect of manganese oxide micromotors: Catalytic degradation and adsorptive bubble separation of organic pollutants, *Chem. Eur. J.* 22 (2016) 1244–1247, <https://doi.org/10.1002/chem.201504474>.
- [46] X. He, Y.K. Bahk, J. Wang, Organic dye removal by MnO₂ and Ag micromotors under various ambient conditions: The comparison between two abatement mechanisms, *Chemosphere* 184 (2017) 601–608, <https://doi.org/10.1016/j.chemosphere.2017.06.011>.
- [47] H. Sun, G. Zhou, S. Liu, H.M. Ang, M.O. Tade, S. Wang, Nano-Fe⁰ encapsulated in microcarbon spheres: Synthesis, characterization, and environmental applications, *ACS Appl. Mater. Interfaces* 4 (2012) 6235–6241, <https://doi.org/10.1021/am301829u>.
- [48] M. Lei, Y. Tang, H. Wang, L. Zhu, G. Zhang, Y. Zhou, H. Tang, A catalytic strategy for rapid cleavage of C-Cl bond under mild conditions: Effects of active hydrogen induced by Pd nanoparticles on the complete dechlorination of chlorobenzenes, *Chem. Eng. J.* 419 (2021), 129510, <https://doi.org/10.1016/j.cej.2021.129510>.
- [49] K. Makino, M.M. Mossoba, P. Riesz, Chemical effects of ultrasound on aqueous-solutions - formation of hydroxyl radicals and hydrogen-atoms, *J. Phys. Chem.* 87 (1983) 1369–1377, <https://doi.org/10.1021/j100231a020>.
- [50] X. He, B. Sun, M. He, H. Chi, Z. Wang, W. Zhang, J. Ma, Highly efficient simultaneous catalytic degradation and defluorination of perfluorooctanoic acid by the H₂O₂-carbon/MnO₂ system generating O₂[•]- and [•]OH synchronously, *Appl. Catal. B* 277 (2020), 119219, <https://doi.org/10.1016/j.apcatb.2020.119219>.
- [51] X. He, B. Li, P. Wang, J. Ma, Novel H₂O₂-MnO₂ system for efficient physico-chemical cleaning of fouled ultrafiltration membranes by simultaneous generation of reactive free radicals and oxygen, *Water Res.* 167 (2019), 115111, <https://doi.org/10.1016/j.watres.2019.115111>.
- [52] K. Villa, J. Viktorova, J. Plutnar, T. Ruml, L. Hoang, M. Pumera, Chemical microrobots as self-propelled microbrushes against dental biofilm, *Cell Rep. Phys. Sci.* 1 (2020), 100181, <https://doi.org/10.1016/j.xcrp.2020.100181>.